WILEY-VCH

Quasi One-dimensional van der Waals Gold Selenide with Strong Interchain Interaction, High Conductivity and Nonsaturating Giant Magnetoresistance

*Jingli Wang, Jingsi Qiao, Kang Xu, Jiewei Chen, Yuda Zhao, Bocheng Qiu, Ziyuan Lin, Wei Ji, and Yang Chai**

Dr. J. Wang, Dr. J. Qiao, K. Xu, J. Chen, Dr. Y. Zhao, Dr. B. Qiu, Z. Lin, Prof. Dr. Y. Chai
Department of Applied Physics, The Hong Kong Polytechnic University, Hung Hom, Kowloon, Hong Kong, P. R. China
E-mail: ychai@polyu.edu.hk

Dr. J. Wang, J. Chen, Dr. B. Qiu, Z. Lin, Prof. Dr. Y. Chai
The Hong Kong Polytechnic University Shenzhen Research Institute, Shenzhen, People's Republic of China

Dr. J. Qiao, Prof. W. Ji
Beijing Key Laboratory of Optoelectronic Functional Materials & MicroNano Devices, Renmin University of China, Beijing, 100872, P. R. China

Keywords: Quasi one-dimensional (1D) materials; two-dimensional (2D) materials; van der Waals; anisotropic; giant magnetoresistance

ABSTRACT- The atomic structure of quasi one-dimensional (1D) van der Waals materials can be regarded as the stacking of atomic chains to form thin flakes or nanoribbons, which substantially differentiates them from typical two-dimensional (2D) layered materials and 1D nanotube/nanowire array. Here we present our studies on a quasi 1D noble metal monochalcogenides, gold selenide (AuSe), which possesses high anisotropic crystal structure and unique physical properties. Our polarized Raman characterizations verify high anisotropy of vibrational behavior of AuSe due to its low in-plane symmetry. Electrically, AuSe exhibit high in-plane conductivity along the directions of both atomic chains and perpendicular one, which can be understood as a result of strong interchain interaction. We found that AuSe is a topologically trivial semimetal and exhibits a near quadratic nonsaturating giant magnetoresistance of 1841% with the magnetic field perpendicular to the in-plane of AuSe. Our works help to establish fundamental understandings on this quasi 1D van der Waals semimetallic AuSe and identify it as a new candidate for exploring the giant magnetoresistance.

Two-dimensional (2D) materials usually exhibit isotropic in-plane physical properties. However, some 2D materials, *e.g.*, black phosphorus and rhenium disulfide, have shown anisotropically physical properties because of their low in-plane symmetry, [1-6] which is a result of strong anisotropy in the chemical bonds. The asymmetric atomic arrangements in these 2D materials give rise to anisotropic electrical mobility, phonon vibrational modes and photo-response, enabling the design of new electronic and optoelectronic devices that cannot be easily realized in isotropic materials. Researchers have demonstrated these anisotropic 2D materials for logic inverter, light polarizers, polarization detectors, piezoelectric applications, and magnetic sensors, *etc.* [2, 3, 7, 8] For the mostly studied 2D anisotropic materials, the in-plane atoms are typically connected by strong chemical bonding.

Recently, researchers have identified some emerging types of quasi one-dimensional (1D) van der Waals (vdWs) materials that are stacked by atomic chains with intrachain chemical bonding and interchain vdWs interaction.[6, 7, 9] Layered selenium and tellurium are quasi 1D vdWs semiconductors, exhibiting extraordinarily high carrier mobility, high optical absorption, intrinsic anisotropy, tunable bandgap, and strong environmental stability.[3, 9] Quasi 1D noble metal monochalcogenides (*e.g.*, AuSe) atomic chains are connected by covalent bonding along the axial direction. These 1D AuSe atomic chains can be stacked together, forming 1D needle-like nanoribbon or 2D nanosheet structure. [10-17] The difference between strong intrachain chemical bonding and interchain interaction leads to high anisotropy in the 1D vdWs material, resulting in thoroughly different properties compared with typical 2D layered materials and 1D nanotubes/nanowires.[18]

In this work, we investigate the quasi 1D vdWs AuSe using optical spectroscopy, electrical characterization and magnetotransport measurement together with density functional theory (DFT) calculations. Polarized-resolved Raman spectra exhibit anisotropic vibration behaviors of AuSe. By electrical measurement, we find that 1D vdWs AuSe shows metallic behaviors with high in-plane conductivity of 7.5×10^5 S m^{-1}, which is comparable to graphene and even some metals. Our DFT calculations show

that AuSe is a topologically trivial semimetal with compensated electrons and holes. The longitudinal magnetoresistance of AuSe exhibits a near quadratic nonsaturating giant magnetoresistance (GMR). The upturn and reentrant metallic behavior can be understood as a result of the carrier mismatch at low temperature. The distinct magnetoresistance (MR) characteristics along different directions of AuSe further verify its anisotropic properties. These studies identify AuSe as a new category of quasi 1D vdWs materials and a new candidate for the GMR.

AuSe possesses two different crystalline structures, namely, α-phase and β-phase, both of which belong to space group *C2h*. α-AuSe is a thermodynamically stable phase, while β-AuSe is a metastable phase. [14, 17, 19] In this work, we mainly focus on the α-phase AuSe. **Figure 1**(a) shows the schematic view of atomic structure of bulk α-phase AuSe. There are two different coordination sites for Au atoms in AuSe, where one is linearly coordinated to two Se atoms, and the other is surrounded by four Se atoms in the form of a planar square. These essential bonds give rise to the formation of 1D atomic chains along the direction of the monoclinic *b*-axis, and these 1D chains are stacked together along the *a*-axis and *c*-axis, forming quasi 1D AuSe. Figure 1(b) and 1(c) present the conventional cell of α-phase AuSe in the forms of 1D chain and bulk form, respectively. As shown in Figure 1(c), these 1D atomic chains shift along the *b*-axis by 0.5*b* relative to the neighboring chain. According to our first-principle calculations, the bulk α-AuSe has the crystal parameters with a = 1.203 nm, b = 0.378 nm, c = 0.845 nm, $\alpha = \gamma = 90°$, $\beta = 101.1°$, in good agreement with previous reports.[12] The interchain binding energy along the *c*-axis and *a*-axis directions are -0.39 eV and -0.68 eV, respectively. This interchain binding energy is much higher than the interlayer binding energy in MoS_2 (-0.24 eV), PtS_2 (-0.28 eV) and lower than that of tellurene (-0.85 eV).[18, 20, 21] This large binding energy (-0.68 eV and -0.39 eV) also implies strongly hybridized interchain Se and Au atoms and strong interchain interaction in neighboring AuSe atomic chains, in analog to the “covalent-like S-S quasi-bonding” in few-layered PtS_2 and $PtSe_2$.[20, 21] The binding energy along the *a*-axis is much higher than that along the *c*-axis, indicating that α-AuSe is most likely to be exfoliated along

the *c*-axis. With the increase of the AuSe thickness, the binding energy shows negligible change, accompanied with negligible change of lattice constant, as shown in **Figure S1**.

Figure 1(d) is a typical optical microscope image of quasi 1D vdWs *α*-phase AuSe flake mechanically exfoliated onto a Si substrate with 300-nm-thickness SiO_2. The exfoliated AuSe flake clearly shows the belt-like shape and sharp edge, indicating the intrinsic characteristics of a quasi 1D vdWs characteristic of AuSe. This feature also makes it easy to identify the chain direction of AuSe along the *b*-axis. Figure 1(e) is the atomic force image (AFM) of the flake, showing the thickness of 33.2 nm. Figure 1(f) is a transmission electron microscopy (TEM) image of AuSe flake. The spacing between the (400) crystal plane is measured to be 0.29 nm. The spacing between (100) plane is calculated to be 1.16 nm, in good agreement with the lattice parameter along the *a*-axis calculated by DFT. The composition and the stoichiometric ratio of the AuSe crystal are characterized by energy-dispersive X-ray (EDX) spectra. The atom ratio between Au and Se atom ratio approximates 1:1, as shown in **Figure S2.**

Raman spectroscopy is of vital importance for the characterization of vdWs materials.[22] The lattice structure of bulk AuSe belongs to the C2/m point group. There are 4 irreducible representations: A_g, B_g, A_u and B_u. The primitive cell of bulk AuSe consists of 8 atoms. In total, there are 24 vibration modes, including 12 Raman active modes (A_g and B_g) and 12 infrared active modes (A_u and B_u). In the high-frequency region, there are three pronounced Raman peaks in the polarization dependent Raman spectra of AuSe under an excitation laser with the wavelength of 488 nm, as shown in **Figure 2**(a). The peaks at 201.7 cm^{-1} and 211.1 cm^{-1} are found to be highly polarized, while the peak at 181.2 cm^{-1} is independent on the polarization. The polarization dependent Raman peaks are out-of-plane modes and the polarization independent Raman peaks are in-plane mode.[20, 21] Figure 2(b) presents the intensity of the peaks (201.7 cm^{-1} and 211.1 cm^{-1}) in the polar axis. First-principle calculations further reveal the schematic diagrams of the vibrational displacement for different Raman peaks. We identify the out-of-plane modes at 201.7 cm^{-1} and 211.1 cm^{-1} as A_g^6 and B_g^4, respectively; and the in-plane mode (B_g^3) is located at 181.2 cm^{-1}.

To explore the structural change of AuSe at low temperature, we performed temperature-dependent Raman of bulk AuSe, as shown in Figure 2(c). The position of all Raman active peaks shows blue-shift approximately 1 cm^{-1} with the decrease of temperature from 293 K to 93 K. The measured temperature dependence of the Raman mode frequency shift can be characterized by a linear equation: $\omega = \omega_0 + \chi T$, where ω_0 is the frequency at 0 K and χ is the first-order temperature coefficient. [23] The measured χ values for the modes of B_g^3, A_g^6 and B_g^4 in a bulk AuSe are -0.015, -0.007, and -0.009 cm^{-1}/K, respectively, as shown in **Figure S3**. This temperature-dependent softening mode is due to the an-harmonic contributions induced by phonon-phonon interactions. [23] Similar results and detailed analysis have been reported for MoS_2. [23] These insignificant changes of Raman spectra indicate negligible structure change of AuSe in this temperature range.

The symmetry of few-layered AuSe and bulk AuSe are different. For few-layered AuSe, the primitive cell contains 16 atoms, while the primitive cell for bulk AuSe has 8 atoms. The symmetry of the primitive cell results in no interlayer shearing and breathing modes in bulk AuSe. In its bulk form, we cannot observe obvious layer-dependent Raman characteristics because the mechanical vibration changes negligibly as a result its low symmetry.[20, 21] Ultralow frequency Raman modes of bulk AuSe represent the relative intralayer motions, which is different from other 2D layered materials (graphene, MoS_2, PtS_2, *etc*). There are 4 observable peaks in the low-frequency Raman spectra of bulk AuSe with excitation laser wavelength of 532 nm, as shown in Figure 2(d). The A_g^2 (34.5cm^{-1}), A_g^3 (41.7 cm^{-1}) and A_g^4 (70.9 cm^{-1}) are polarized dependent, but the B_g^1 (16.7 cm^{-1}) mode is polarized independent, indicating that A_g^2, A_g^3 and A_g^4 are out-of-plane modes, while mode B_g^1 is an in-plane mode. All the Raman mode are given in **Table S1** and **Figure S4**.

Figure 3(a) shows three-dimensional (3D) Brillouin zone of bulk α-AuSe. In its 1D form, the AuSe atomic chain is an indirect bandgap semiconductor with a bandgap of 1.26 eV (Figure 3(b)). Both the conduction band minimum (CBM) and valence band maximum (VBM) of AuSe locate between the G and Y point. Figure 3(c) presents the

bandstructure of bulk α-phase 1D vdWs AuSe. There are two hole pockets (α and β) locating in *G* and two electron pockets (γ and δ) locating between G and Y. The band edge of δ locates at the Fermi level. These results suggest that two types of carriers exist in AuSe. AuSe belong to *C2h*, the cross point in G-Y point only satisfy the symmetry of *C2*. Considering spin-orbital coupling, the cross point represents the same irreducible representation. As a result, there will be a gap at the cross point. In this regard, bulk AuSe is a topologically trivial semimetal. The bandstructures of the monolayer, 2-layer and 4-layer AuSe are given in **Figure S5** and **S6**.

To study the electrical properties of the AuSe, we mechanically exfoliated AuSe flakes onto Si substrate with 300 nm SiO_2 and prepared metal electrodes onto the AuSe flakes. Figure 3(d) is the current-voltage (I-V) characteristics of the bulk AuSe. The I-V curves show linear relationships without any gate control, further confirming metallic behaviors of bulk AuSe crystal. **Figure S7** presents the temperature-dependent I-V curves of another bulk AuSe at 300 K and 50 K, exhibiting metallic characteristics. The current along different directions of the AuSe flake with $V_g = 0$ V is given in **Figure S8**. The two-terminal conductance along the direction of the AuSe atomic chain (the *b*-axis in Figure 1c) is 1.8×10^{-3} S, and the conductance perpendicular to the AuSe atomic chain (the *a*-axis in Figure 1c) is 1.48×10^{-4} S. The high conductivity perpendicular to the *b*-axis indicates strong interchain interaction between AuSe atomic chains, which is consistent with the quasi covalent bond like interaction along the *a*-axis of AuSe.

Figure 3(e) shows the extracted 4-terminal conductivity along the *b*-axis ($\sigma = \frac{I_{ds}}{\Delta V}\frac{L}{W}$) of quasi 1D vdWs AuSe with different thicknesses as a function of temperature from 50 K to 293 K, where I_{ds} is the current, *V* is the voltage drop, and *L/W* is the length/width ratio of the channel. For a bulk AuSe crystal with a thickness of 102 nm, the conductivity at room temperature is 7.5×10^5 S m^{-1}, which is even larger than that of graphene ($0.2\sim2\times10^6$ S m^{-1}) and $PtSe_2$ (6.2×10^5 S m^{-1}) and comparable to many metals [24]. When the temperature decreases to 50 K, the conductivity increases to 5.9×10^6 S m^{-1}. For 20-nm-thick AuSe, the conductivity increases from 1.7×10^4 S m^{-1} (250 K) to 6.5×10^4 S m^{-1}(50 K). The conductivity of all the AuSe samples increases with the

decrease of the temperature, which is due to the reduced electron-phonon scattering at low temperature. Figure 3(f) is the comparison of the conductivity of AuSe and other highly conductive materials, manifesting its high electrical conductivity [21, 25-31].

Furthermore, we performed magnetotransport studies to reveal the carrier transport of AuSe. **Figure 4**(a) presents the longitudinal resistivity (ρ_{xx}, along the atomic chain direction *b*-axis) of AuSe as a function of temperature with magnetic field from 0 T to 9 T, where the direction of magnetic fields is perpendicular to the *a*-*b* plane of AuSe, and the current is collected along the *b*-axis of AuSe. The ρ_{xx} of AuSe at zero field shows metallic behavior from 2 K to 300 K. The AFM image (**Figure S9**(a)) of this AuSe device shows its thickness of 56 nm. At the temperature of 70 K, the ρ_{xx} of AuSe shows an obvious upturn under the magnetic field of 9 T. The change rate of ρ_{xx} (**Figure S10**(a)) as a function of temperature shows that the minima of the upturn under 6 T and 9 T are 37.4 K and 68.7 K, respectively. Figure S10(b)-(c) shows the magnetoresistance (MR) and the normalized MR as a function of the temperature. The normalized MR shows almost the same temperature dependence under different magnetic fields, indicating that this upturn is not caused by the magnetic field induced metal-insulator transition [32-34]. A drop of the ρ_{xx} of AuSe is observed from 30 K to 2 K under a magnetic field of 9 T. Although the reentrant metallic behavior is usually observed in some semimetals when the Weyl nodes are identified in the vicinity of the Fermi level, *e.g.,* graphene, NbP and TaAs [35, 36]. However, a similar result for semimetal with the upturn effect was only reported in WP_2 [32, 34, 37].

Figure 4(b) shows the longitudinal MR ($MR = \Delta\rho(H)/\rho_0$) of AuSe. The MR exhibits near quadratic dependence on the magnetic field, reaching 1557% at 2 K and 9 T, and showing unsaturation trend up to the highest field in our measurements. Figure 4(c) is Kohler's plot ($MR = \alpha\,(B/\rho_{xx}(T,0))^m$), showing a single straight line with $m \sim 2$ for temperature higher than 50 K. When the temperature is below 50 K, the index *m* is much smaller than 2. At 2 K, the index *m* drops to 1.36. Comparable *m* values were reported in LaSb of 1.78 and LaAs of 1.35[38-40]. The Kohler's plot of another sample with a thickness of 102 nm is given in **Figure S11**(a)-(b).

According to the DFT calculation (Figure 3(b)), two hole pockets locate in G point and two electron pockets locate between G-Y point, respectively. The Hall resistance ρ_{xy} of AuSe (Figure 4(d)-(e)) exhibits nonlinear characteristics under low magnetic field, indicating the existence of carrier compensation. Hall angle is typically used to identify charge compensation and energy dispersion in materials with nonsaturating MR [35]. **Figure S12** shows the Hall angle of an AuSe device as a function of temperature. The Hall angle of AuSe is close to zero from 2 K to 300 K, indicating that the electron and hole of AuSe are most likely to be compensated [35]. Considering both electron and hole participate in the carrier transport, we adopt two-band model to extract the carrier mobility of AuSe. The Hall conductivity σ_{xy} and longitudinal conductivity σ_{xx} can be calculated from equation (1):

$$\sigma_{xy} = \frac{\rho_{yx}}{\rho_{xx}^2+\rho_{xy}^2}, \quad \sigma_{xx} = \frac{\rho_{xx}}{\rho_{xx}^2+\rho_{xy}^2} \qquad (1)$$

where the ρ_{xx} and ρ_{xy} are the longitudinal and Hall resistance [35]. We can fit the Hall conductivity σ_{xy} and longitudinal conductivity σ_{xx} from equations (2) and (3):

$$\sigma_{xy} = \left(\frac{n_h\mu_h^2}{1+\mu_h^2H^2} - \frac{n_e\mu_e^2}{1+\mu_e^2H^2}\right)eB, \qquad (2)$$

$$\sigma_{xx} = \left(\frac{\mu_h n_h}{1+\mu_h^2H^2} + \frac{\mu_e n_e}{1+\mu_e^2H^2}\right)e \qquad (3)$$

where the n_h, μ_h, n_e, μ_e are the carrier concentration and mobility of hole and electron, respectively [39, 41]. All the data of the MR and the Hall resistance can be fitted into these two equations. The carrier density obtained from the two-band model fitting are 1.2×10^{20} cm^{-3} (hole) and 1.067×10^{20} cm^{-3} (electron) at 2 K, respectively. The ratio of n_h/n_e is 1.12, showing a small compensation mismatch between the electron and the hole. The n_h/n_e ratio approaches 1 with temperature up to 300 K. Based on the DFT calculation, the carrier density of the two hole pockets are 1.5 and 5.5×10^{21} cm^{-3} and the carrier density of the electron pocket is 6.6 and 0.4×10^{20} cm^{-3}. The fitting curve of the σ_{xy} and the ρ_{xx} are given in **Figure S13**. The carrier density and the mobility are documented in **Table 1**. Both the DFT calculation and the two-band model fitting indicate that AuSe shows well electron-hole compensation. The large mobility and the compensated carrier all contribute to the giant nonsaturating parabolic MR in AuSe.

Figure S14 shows the theoretical simulation of ρ_{xx} of AuSe as a function of temperature. Even without taking the mobility into consideration, it clearly shows the upturn and the reentrant metallic behavior, matching experimental results very well. If the carriers are compensated, the MR will follow the Kohler's law perfectly under all temperature and the reentrant metallic behavior will disappear.

In addition, we characterize the magnetotransport properties of AuSe by applying magnetic field with different directions. **Figure 5**(a) shows the schematic device configuration with the illustration of the direction of magnetic fields. We define the *y*-axis along the current direction (also the *b*-axis of the AuSe atomic chain), *x*-axis perpendicular to AuSe chain within the plane (also the *a*-axis in Figure 1c), and *z*-axis perpendicular to the *a*-*b* plane. Figure S9(c) is the AFM image of this device. Figure 5(b) shows the angle-dependent ρ_{xx} of AuSe under different temperature, where the magnitude of the magnetic field is fixed at 9 T and the direction is changed continuously from B_x field (0 degree) to B_z field (90 degree). The ρ_{xx} changes from 0.004 mΩ·cm (0 degree) to 0.0473 mΩ·cm (90 degree) at 2 K, and from 0.0198 mΩ·cm (0 degree) to 0.074 mΩ·cm (90 degree) at 50 K. Figure 5(c) shows the ρ_{xx} with the direction of magnetic field varied continuously from B_y field (0 degree) to B_z field (90 degree) when the magnitude of the magnetic field is fixed at 9 T. The ρ_{xx} changes from 0.0035 mΩ·cm (0 degree) to 0.048 mΩ·cm (90 degree) under 2 K, and from 0.017 mΩ·cm (0 degree) to 0.080 mΩ·cm (0 degree) at the temperature of 50 K. These results further confirm the anisotropic MR in quasi 1D AuSe and indicate a nonspherical Fermi surface of bulk AuSe.

Figure 5(d) is the longitudinal resistance of the AuSe when the magnetic field is perpendicular to the *a*-*b* plane along the *z*-axis. The AuSe device exhibits GMR of 1841% at 2 K. Figure 5(e) is the ρ_{xx} with the magnetic field along the *y*-axis (the direction of the AuSe atomic chain). Negligible change in ρ_{xx} is observed when the magnetic field changes from -9 T to 9 T. Then we change the direction of magnetic field to the *x*-axis, which is perpendicular to the AuSe atomic chain within the *a*-*b* plane. The ρ_{xx} is given in Figure 5(f). The MR of AuSe under 50 K shows a significant decrease from 373%

down to 22%. In a stark contrast, the MR of AuSe under 2 K, 4 K and 10 K, decrease to zero, which is quite different from the MR when the magnetic field is along the B_z direction and requires further investigations.

In summary, we perform systematic investigation on quasi 1D metallic AuSe using optical spectroscopies, electrical characterization and magnetotransport measurement. The quasi 1D nature of AuSe makes it a highly anisotropic material, exhibiting polarization dependent vibration behavior and highly anisotropic MR. Magnetotransport measurement and theoretical calculations show that AuSe is a topologically trivial semimetal with GMR. The carrier is compensated over a wide temperature range. A small carrier mismatch at low temperature results in the upturn and reentrant metallic behavior at low temperature. These studies helps to enrich the vdWs materials family and identify the quasi 1D vdWs materials as a promising category for anisotropic characteristics and GMR characteristics.

Experimental Section

Device fabrication and electrical characterization. AuSe single crystals were purchased from HQ graphene. Crystals were cleaved into small pieces and transferred onto Scotch tape. The samples were transferred onto the Si substrate with 300-nm-thick SiO_2 for Raman tests and device fabrication. The substrates were spin-coated with MMA and PMMA for subsequent electron beam lithography. Metal electrodes were deposited onto thin AuSe flakes by sequential electron-beam evaporation of Ti (10 nm) and Au (60 nm) at the rates of 0.5 Å /s and 0.7 Å /s. Temperature-dependent electrical measurements were carried out by a Keithley 4200 semiconductor parameter analyzer in a closed-cycle cryogenic probe station with a base pressure of 10^{-5} Torr.

Material characterization. A micro Raman spectrometer (HORIBA HR800) was used for high-frequency, and Witec Raman system was used for the low-frequency Raman test. The AuSe flakes were transferred onto copper grids by KOH etching method. STEM image was captured by FEI Tecnai F20 operated with an acceleration voltage of 200 kV. The Raman scattering intensity is proportional to $|e_s \cdot R \cdot e_i|^2$, where e_i is the

incident beam (*cosθ, sinθ, 0*), and e_s is the scattered light (1, 0, 0). The Raman tensor of C2/m can be represented by :

$$R_{Ag} = \begin{pmatrix} a & 0 & d \\ & b & \\ d & & c \end{pmatrix},$$

$$R_{Bg} = \begin{pmatrix} & e & \\ e & & f \\ & f & \end{pmatrix},$$

By substituting the unitary vectors and the Raman tensors defined above, we can obtain the analytical expressions for the angle-dependent intensities of the A_g and B_g peaks:

$$S_{Ag}=a^2cos\theta^2,$$

$$S_{Bg}=e^2sin\theta^2,$$

DFT calculations. DFT calculations were performed using the generalized gradient approximation for the exchange-correlation potential, the projector augmented wave method [42, 43] and a plane-wave basis set as implemented in the Vienna *ab-initio* simulation package (VASP) [44] and Quantum Espresso (QE) [45]. Density functional perturbation theory was employed to calculate phonon-related properties, including Raman intensity (QE), activity (QE) and shifts (VASP). In terms of VASP calculations, the kinetic energy cut-off for the plane-wave basis set was set to 600 eV for geometric optimizations and vibrational properties calculations while 500 eV for electronic structure calculations. For QE calculations, the kinetic energy cut-off was set 50 Ry and 600 Ry for wavefunction and charge density, respectively. A *k*-mesh of 5×15×7 was adopted to sample the first Brillouin zone of the conventional unit cell of bulk AuSe in all calculations. The mesh density of *k* points was kept fixed in calculations of bulk AuSe and 1D AuSe chain. In atomic structure optimization and vibrational property calculations, van der Waals interactions were considered at the vdW-DF [46, 47] level with the optB6b exchange functional (optB86b-vdW) [48-50], which was proved to be accurate in describing the structural properties of layered materials[18, 51-53]. The shape and volume of each supercell were fully optimized and all atoms in the supercell were allowed to relax until the residual force per atom was less than 5×10^{-3} eV·Å^{-1}. Electronic bandstructures were calculated using the PBE functional with and without the inclusion of spin-orbit coupling.

Acknowledgement

J. Wang and J. Qiao contributed equally to this work. This work was supported by the Research Grant Council of Hong Kong (N_PolyU540/17), the Shenzhen Science and Technology Innovation Commission (20180038), and the Hong Kong Polytechnic University (G-SB53 and G-YBPS).

Received: ((will be filled in by the editorial staff))

Revised: ((will be filled in by the editorial staff))

Published online: ((will be filled in by the editorial staff))

References

[1] K. Wang, D. Graf, L. Li, L. Wang, C. Petrovic, Sci. rep. 2014, 4, 7328.
[2] Q. Li, K. Xie, D. Yuan, Z. Wei, L. Hu, Q. Mao, H. Jiang, Z. Hu, E. Wang, Appl. Opt. 2016, 55, 8541.
[3] Y. C. Du, G. Qiu, Y. X. Wang, M. W. Si, X. F. Xu, W. Z. Wu, P. D. D. Ye, Nano. Lett. 2017, 17, 3965.
[4] S. J. Yang, H. Cai, B. Chen, C. Ko, V. O. Ozcelik, D. F. Ogletree, C. E. White, Y. X. Shen, S. Tongay, Nanoscale 2017, 9, 12288.
[5] A. Pariari, R. Singha, S. Roy, B. Satpati, P. Mandal, Sci. rep. 2018, 8, 10527.
[6] W. Zhang, Q. S. Wu, O. V. Yazyev, H. M. Weng, Z. X. Guo, W. D. Cheng, G. L. Chai, Phys. Rev. B 2018, 98.
[7] Y. X. Wang, G. Qiu, R. X. Wang, S. Y. Huang, Q. X. Wang, Y. Y. Liu, Y. C. Du, W. A. Goddard, M. J. Kim, X. F. Xu, P. D. Ye, W. Z. Wu, Nat. Electro. 2018, 1, 228.
[8] E. F. Liu, Y. J. Fu, Y. J. Wang, Y. Q. Feng, H. M. Liu, X. G. Wan, W. Zhou, B. G. Wang, L. B. Shao, C. H. Ho, Y. S. Huang, Z. Y. Cao, L. G. Wang, A. D. Li, J. W. Zeng, F. Q. Song, X. R. Wang, Y. Shi, H. T. Yuan, H. Y. Hwang, Y. Cui, F. Miao, D. Y. Xing, Nat. Comm. 2015, 6.
[9] J. K. Qin, G. Qiu, J. Jian, H. Zhou, L. M. Yang, A. Charnas, D. Y. Zemlyanov, C. Y. Xu, X. F. Xu, W. Z. Wu, H. Y. Wang, P. D. D. Ye, Acs Nano 2017, 11, 10222.
[10] M. M. Srivastava, Srivasta.N, Zeitschrift Fur Metallkunde 1971, 62, 614.
[11] O. N. Srivastava, M. M. Srivastava, Zeitschrift Fur Metallkunde 1972, 63, 158.
[12] A. Rabenau, H. Schulz, J.Of the Less-Common Metals 1976, 48, 89.
[13] S. Nath, A. Pal, S. K. Ghosh, S. Praharaj, S. Panigrahi, S. Kundu, T. Thundat, T. Pal, J. Of Nanos. And Nanotec. 2005, 5, 1832.
[14] L. F. E. Machogo, P. Tetyana, R. Sithole, S. S. Gqoba, N. Phao, M. Airo, P. M. Shumbula, M. J. Moloto, N. Moloto, Appl. Surf. Sci. 2018, 456, 973.
[15] D. Feng, P. Taskinen, J.Of Chem. Thermo. 2014, 71, 98.
[16] X. L. Xu, W. K. Chen, X. Wang, B. Z. Sun, Y. Li, C. H. Lu, Chinese J. Of Chem.2008, 26, 107.

[17] F. E. Wagner, P. Palade, J. Friedl, G. Filoti, N. Wang, in *International Conference on the Applications Of the Mossbauer Effect*, Vol. 217 (Eds: H. Muller, M. Reissner, W. Steiner, G. Wiesinger), 2010.
[18] J. Qiao, Y. Pan, F. Yang, C. Wang, Y. Chai, W. Ji, Sci. Bull.2018, 63, 159.
[19] A. Rabenau, H. Schulz, Acta Crystallographica Section A 1975, 31, S67.
[20] Y. Zhao, J. Qiao, P. Yu, Z. Hu, Z. Lin, S. P. Lau, Z. Liu, W. Ji, Y. Chai, Adv. Mater. 2016, 28, 2399.
[21] Y. Zhao, J. Qiao, Z. Yu, P. Yu, K. Xu, S. P. Lau, W. Zhou, Z. Liu, X. Wang, W. Ji, Y. Chai, Adv. Mater.2017, 29.
[22] Y. Guo, W. Zhang, H. Wu, J. Han, Y. Zhang, S. Lin, C. Liu, K. Xu, J. Qiao, W. Ji, Sci. adv. 2018, 4, eaau6252.
[23] S. Zhang, J. Yang, R. Xu, F. Wang, W. Li, M. Ghufran, Y.-W. Zhang, Z. Yu, G. Zhang, Q. Qin, ACS nano 2014, 8, 9590.
[24] S. Hao, J. W. Zeng, T. Xu, X. Cong, C. Y. Wang, C. C. Wu, Y. J. Wang, X. W. Liu, T. J. Cao, G. X. Su, L. X. Jia, Z. T. Wu, Q. Lin, L. L. Zhang, S. N. Yan, M. F. Guo, Z. L. Wang, P. H. Tan, L. T. Sun, Z. H. Ni, S. J. Liang, X. Y. Cui, F. Miao, Adv. Func. Mater. 2018, 28.
[25] M. Acerce, D. Voiry, M. Chhowalla, Nat. Nanotech. 2015, 10, 313.
[26] R. Raccichini, A. Varzi, S. Passerini, B. Scrosati, Nat. Mater. 2015, 14, 271.
[27] Z. Zhang, J. Niu, P. Yang, Y. Gong, Q. Ji, J. Shi, Q. Fang, S. Jiang, H. Li, X. Zhou, L. Gu, X. Wu, Y. Zhang, Adv. Mater. 2017, 29.
[28] Q. Ji, C. Li, J. Wang, J. Niu, Y. Gong, Z. Zhang, Q. Fang, Y. Zhang, J. Shi, L. Liao, X. Wu, L. Gu, Z. Liu, Y. Zhang, Nano Lett. 2017, 17, 4908.
[29] S. Hao, J. Zeng, T. Xu, X. Cong, C. Wang, C. Wu, Y. Wang, X. Liu, T. Cao, G. Su, L. Jia, Z. Wu, Q. Lin, L. Zhang, S. Yan, M. Guo, Z. Wang, P. Tan, L. Sun, Z. Ni, S.-J. Liang, X. Cui, F. Miao, Adv. Func. Mater.2018, 28, 1803746.
[30] R. A. Matula, Journal of Physical and Chemical Reference Data 1979, 8, 1147.
[31] J. Du, Z. Lou, S. Zhang, Y. Zhou, B. Xu, Q. Chen, Y. Tang, S. Chen, H. Chen, Q. Zhu, H. Wang, J. Yang, Q. Wu, O. V. Yazyev, M. Fang, Phys. Rev. B 2018, 97.
[32] N. Kumar, Y. Sun, N. Xu, K. Manna, M. Yao, V. Suss, I. Leermakers, O. Young, T. Forster, M. Schmidt, H. Borrmann, B. Yan, U. Zeitler, M. Shi, C. Felser, C. Shekhar, Nat. Commun. 2017, 8, 1642.
[33] F. Fallah Tafti, Q. Gibson, S. Kushwaha, J. W. Krizan, N. Haldolaarachchige, R. J. Cava, Proc. of the Natl. Acad. of Sci. 2016, 113, E3475.
[34] V. Nagpal, P. Kumar, Sudesh, S. Patnaik, 2018.
[35] I. A. Leahy, Y. P. Lin, P. E. Siegfried, A. C. Treglia, J. C. W. Song, R. M. Nandkishore, M. Lee, Proc. Natl Acad. Sci. U S A 2018, 115, 10570.
[36] X. C. Huang, L. X. Zhao, Y. J. Long, P. P. Wang, D. Chen, Z. H. Yang, H. Liang, M. Q. Xue, H. M. Weng, Z. Fang, X. Dai, G. F. Chen, Phys. Rev. X 2015, 5.
[37] Y.-Y. Lv, X. Li, J. Zhang, B. Pang, S.-S. Chen, L. Cao, B.-B. Zhang, D. Lin, Y. B. Chen, S.-H. Yao, J. Zhou, S.-T. Zhang, M.-H. Lu, M. Tian, Y.-F. Chen, Phys. Rev. B 2018, 97.
[38] F. F. Tafti, Q. D. Gibson, S. K. Kushwaha, N. Haldolaarachchige, R. J. Cava, Nat. Phys. 2015, 12, 272.
[39] S. Sun, Q. Wang, P.-J. Guo, K. Liu, H. Lei, New J. of Phys. 2016, 18.

[40] L. K. Zeng, R. Lou, D. S. Wu, Q. N. Xu, P. J. Guo, L. Y. Kong, Y. G. Zhong, J. Z. Ma, B. B. Fu, P. Richard, P. Wang, G. T. Liu, L. Lu, Y. B. Huang, C. Fang, S. S. Sun, Q. Wang, L. Wang, Y. G. Shi, H. M. Weng, H. C. Lei, K. Liu, S. C. Wang, T. Qian, J. L. Luo, H. Ding, Phys. Re.letters 2016, 117, 127204.
[41] H. Y. Yang, T. Nummy, H. Li, S. Jaszewski, M. Abramchuk, D. S. Dessau, F. Tafti, Phys. Rev. B 2017, 96.
[42] P. E. Blöchl, Phys. Rev. B 1994, 50, 17953.
[43] G. Kresse, D. Joubert, Phys. Rev. B 1999, 59, 1758.
[44] G. Kresse, J. Furthmüller, Phys. Rev. B 1996, 54, 11169.
[45] P. Giannozzi, S. Baroni, N. Bonini, M. Calandra, R. Car, C. Cavazzoni, D. Ceresoli, G. L. Chiarotti, M. Cococcioni, I. Dabo, A. Dal Corso, S. de Gironcoli, S. Fabris, G. Fratesi, R. Gebauer, U. Gerstmann, C. Gougoussis, A. Kokalj, M. Lazzeri, L. Martin-Samos, N. Marzari, F. Mauri, R. Mazzarello, S. Paolini, A. Pasquarello, L. Paulatto, C. Sbraccia, S. Scandolo, G. Sclauzero, A. P. Seitsonen, A. Smogunov, P. Umari, R. M. Wentzcovitch, J. of Phys.: Cond. Mat. 2009, 21, 395502.
[46] M. Dion, H. Rydberg, E. Schröder, D. C. Langreth, B. I. Lundqvist, Phys. Rev. Lett. 2004, 92, 246401.
[47] K. Lee, É. D. Murray, L. Kong, B. I. Lundqvist, D. C. Langreth, Phys. Rev. B 2010, 82, 081101.
[48] J. Klimes, D. R. Bowler, A. Michaelides, J. of Phys.: Cond. Mat. 2010, 22, 022201.
[49] J. Klimeš, D. R. Bowler, A. Michaelides, Phys. Rev. B 2011, 83, 195131.
[50] T. Thonhauser, V. R. Cooper, S. Li, A. Puzder, P. Hyldgaard, D. C. Langreth, Phys. Rev.B 2007, 76, 125112.
[51] Z.-X. Hu, X. Kong, J. Qiao, B. Normand, W. Ji, Nanoscale 2016, 8, 2740.
[52] J. Hong, C. Wang, H. Liu, X. Ren, J. Chen, G. Wang, J. Jia, M. Xie, C. Jin, W. Ji, Nano lett.2017, 17, 6653.
[53] C. Wang, X. Zhou, Y. Pan, J. Qiao, X. Kong, C.-C. Kaun, W. Ji, Phys. Rev.B 2018, 97, 245409.

Figure and captions

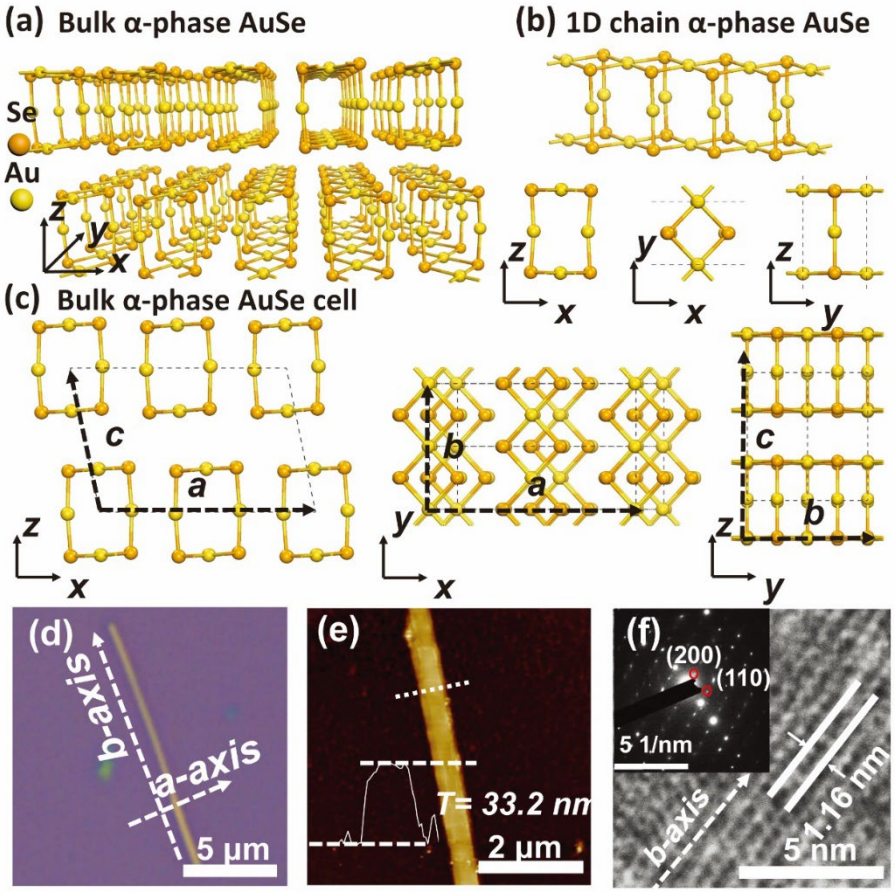

Figure 1. (a) Schematic three-dimensional drawing of crystal structure of bulk α-AuSe. (b) Structure of the 1D atomic chain of α-AuSe. (c) Bulk α-AuSe cell. The DFT calculated lattice parameters are $\alpha = \gamma = 90°$, $\beta = 101.1°$. (d) Optical microscopy image of α-AuSe exfoliated onto 300 nm SiO_2. The scale bar is 5 μm. (e) Atomic force microscopy image of the AuSe flake in (d). The scale bae is 2 μm. (f) TEM image and SAED pattern of the AuSe crystal with the [001] direction. The diffraction pattern shows that the AuSe sample is well crystallized with monoclinic lattice structure.

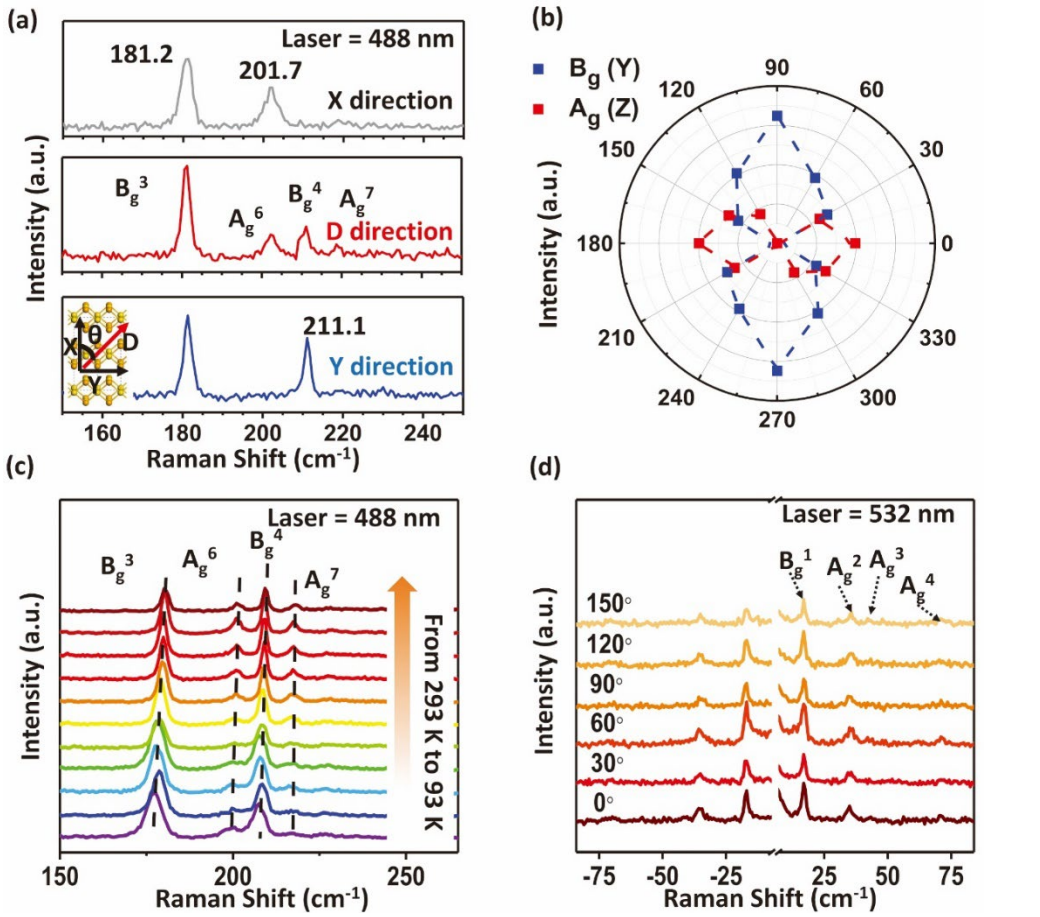

Figure 2. (a) Polarized-resolved Raman spectra of AuSe with 488-nm linearly polarized excitation laser incident from the *z* direction. Raman spectra with an excitation laser polarized along Y-, D- and X- directions. The D direction is along 45° relative to the *x* and *y* directions, as shown in the middle panel. The peak positions show negligible change as a function of the angle. (b) Summarized intensity of the B_g^4 and A_g^6 modes as a function of the polarization of the light. The degree corresponds to the X-direction (*a*-axis) in Figure 2a. (c) Schematic diagram of vibrational displacement for the calculated high frequency Raman mode in *α*-AuSe. (d) Polarized-resolved low-frequency Raman spectra of AuSe. The low-frequency Raman mode also represents the relative intralayer vibrations.

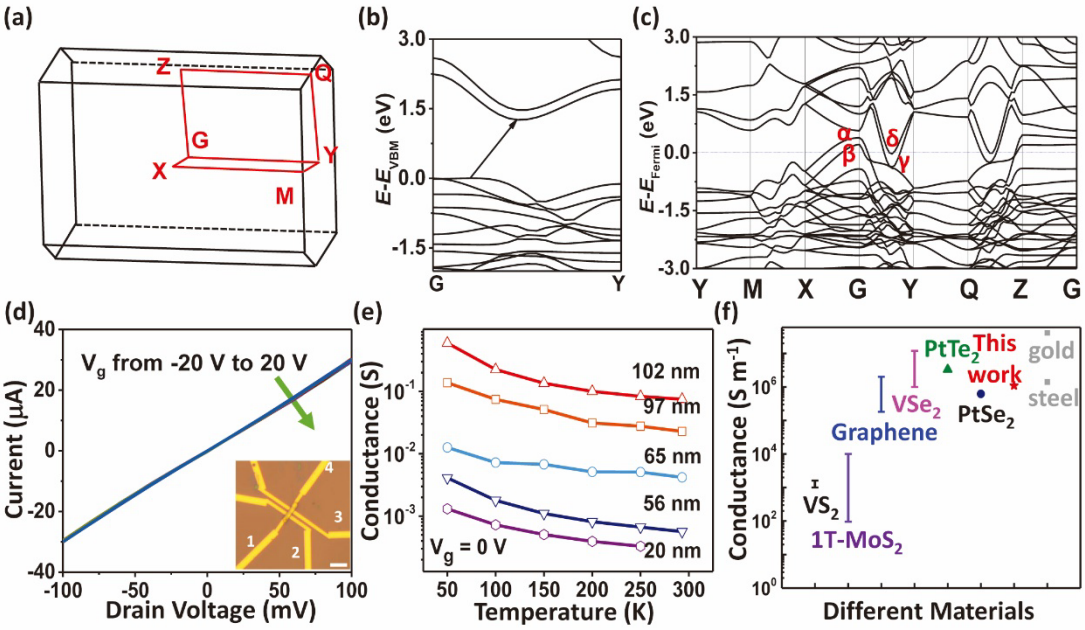

Figure 3. (a) Three-dimensional Brillouin zone of bulk α-AuSe. Bandstructures of (b) 1D AuSe atomic chain and (c) bulk *α*-AuSe. (d) Current-voltage characteristics of Bulk AuSe. The contact electrode is 10 nm Ti and 60 nm Au. Inset is the optical microscopy image of AuSe device on SiO_2/Si substrate. The scale bar is 5 μm. (e) The plot of the 4-terminal conductivity along the *b*-axis of 20, 56, 65, 97 and 102 nm samples with the temperature from 50 K to 300 K. (f) Comparisons of the electrical conductivity among various conductive materials.

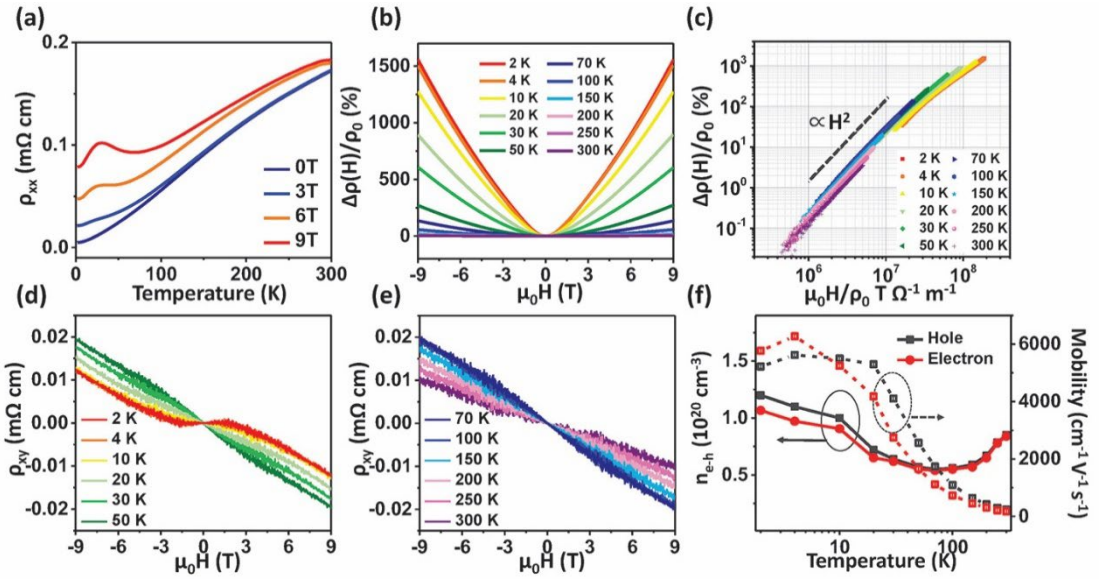

Figure 4. Magnetotransport of AuSe with the magneto field perpendicular to the *a*-*b* plane. (a) Temperature-dependent longitudinal resistance and magnetoresistance of AuSe thin films with a fixed magnetic field from 0 to 9 T perpendicular to the *a*-*b* plane. The resistivities of AuSe at room temperature and 2 K are 0.18 mΩ·cm and 0.005 mΩ·cm, respectively. (b) Longitudinal MR of AuSe thin film with varied magnetic field with the temperature from 2 K to 300 K. (c) Kohler's plot of AuSe from 2 K to 300 K. (d)-(e) Hall resistance of AuSe thin film with varied magnetic field from -9 T to 9 T and temperature from 2 K to 300 K. (f) Carrier density and mobility of AuSe under different temperature. It is noteworthy that the minimum of the carrier density locates at 70 K.

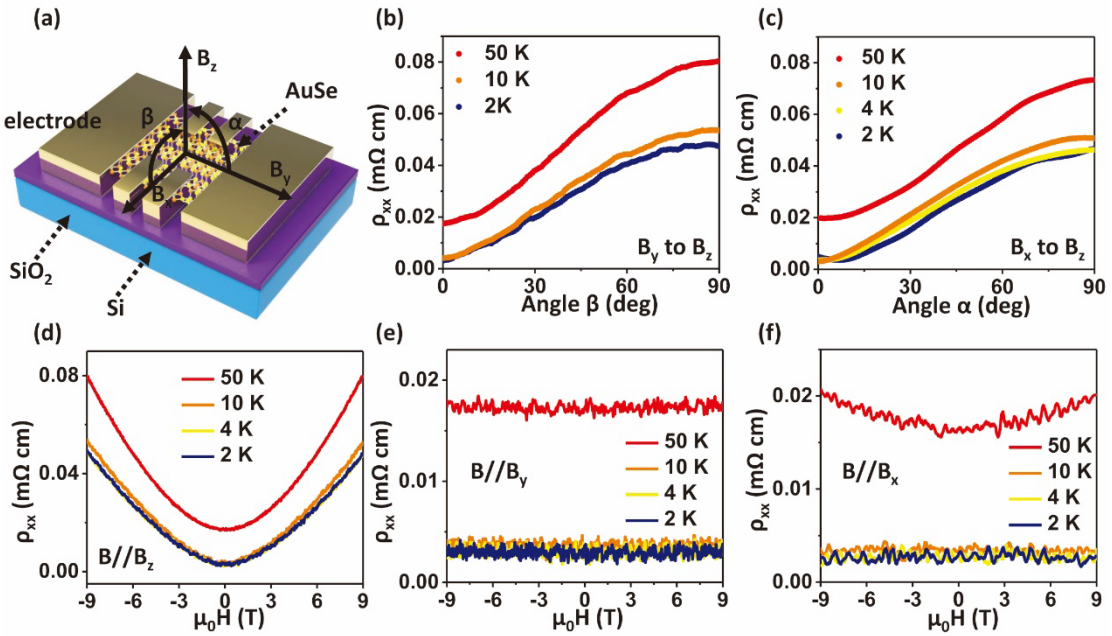

Figure 5. Anisotropic magnetotransport of AuSe. (a) Device scheme configuration and magnetic field setup for the angle-dependent magnetoresistance measurement. The thickness of this sample is 102 nm. (b) Angle-dependent ρ_{xx} when the magnitude of the magnetic field is fixed at 9 T and the direction varied continuously from B_y field (0 degree) to B_z field (90 degree). (c) Angle-dependent ρ_{xx} when the magnitude of the magnetic field is fixed at 9 T and the direction varied continuously from B_x field (0 degree) to B_z field (90 degree). (d) Longitudinal resistance ρ_{xx} of AuSe flake with varied magnetic field from 2 K to 50 K along with B_z (d), B_y (e) and B_x (f).

Table 1. Carrier density of AuSe from DFT calculations and experimental extraction.

	Carrier type	n (10^{20} cm^{-3})	n (10^{20} cm^{-3}) calculation	n (10^{20} cm^{-3}) experiment
Band α	Hole	1.5	7.0	1.2
Band β		5.5		
Band γ	electron	6.6	6.9	1.067
Band δ		0.4		

Quasi One-dimensional van der Waals Gold Selenide with Strong Interchain Interaction, High Conductivity and Nonsaturating Giant Magnetoresistance

*Jingli Wang, Jingsi Qiao, Kang Xu, Jiewei Chen, Yuda Zhao, Bocheng Qiu, Ziyuan Lin, Wei Ji, and Yang Chai**

Dr. J. Wang, Dr. J. Qiao, K. Xu, J. Chen, Dr. Y. Zhao, Dr. B. Qiu, Z. Lin, Prof. Dr. Y. Chai
Department of Applied Physics, The Hong Kong Polytechnic University, Hung Hom, Kowloon, Hong Kong, P. R. China
E-mail: ychai@polyu.edu.hk

Dr. J. Wang, J. Chen, Dr. B. Qiu, Z. Lin, Prof. Dr. Y. Chai
The Hong Kong Polytechnic University Shenzhen Research Institute, Shenzhen, People's Republic of China

Dr. J. Qiao, Prof. W. Ji
Beijing Key Laboratory of Optoelectronic Functional Materials & MicroNano Devices, Renmin University of China, Beijing, 100872, P. R. China

Keywords: Quasi one-dimensional (1D) materials; two-dimensional (2D) materials; van der Waals; anisotropic; giant magnetoresistance

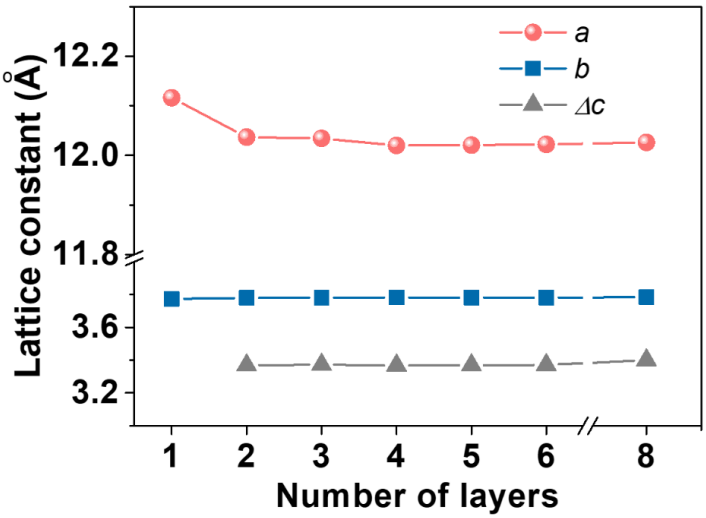

Figure S1. Lattice constant of AuSe as a function of layer number. The lattice constant *b* (along the chain direction) and the interlayer distance *Δc* remain almost unchanged as a function of different number of layers. The lattice constant *a* (perpendicular to the chain direction and within the *a*-*b* plane) reduces with the increase of number of layer.

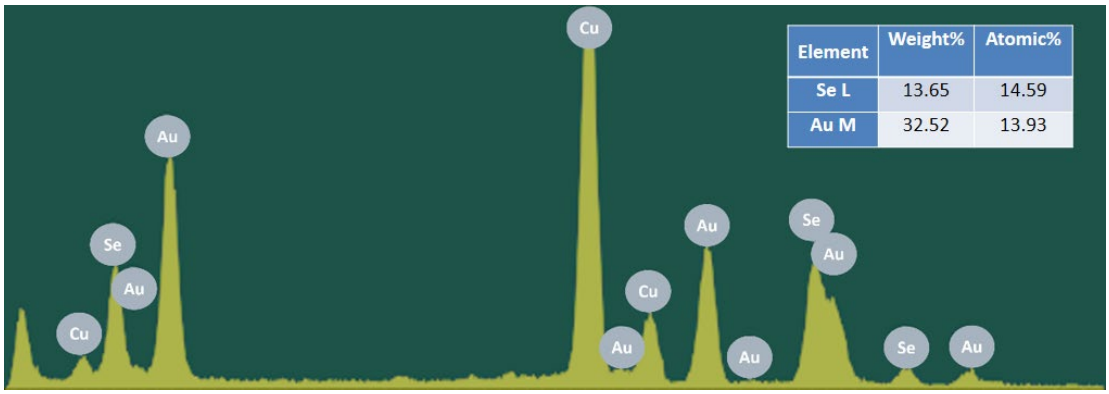

Figure S2. Element distribution of AuSe. The atomic distribution is 51.2:48.8, which is very close to 1:1. The Cu peak observed in this measurement is a result of the Cu grid used in the TEM.

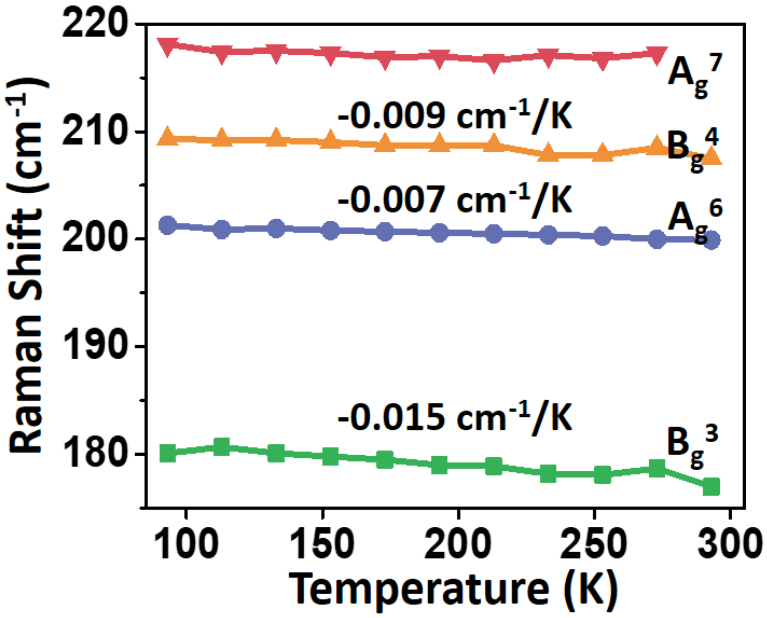

Figure S3. Temperature-dependent Raman peaks of AuSe measured from 93 K to 293 K. The frequency of all Raman active peaks exhibits blue-shift for approximately 2 cm^{-1} with the temperature decreasing from 293 K to 93 K. The change of Raman shift with temperature is determined by the anharmonic terms in the lattice potential energy, which is related to the anharmonic potential constants, the phonon occupation number, and the thermal expansion of the crystal.

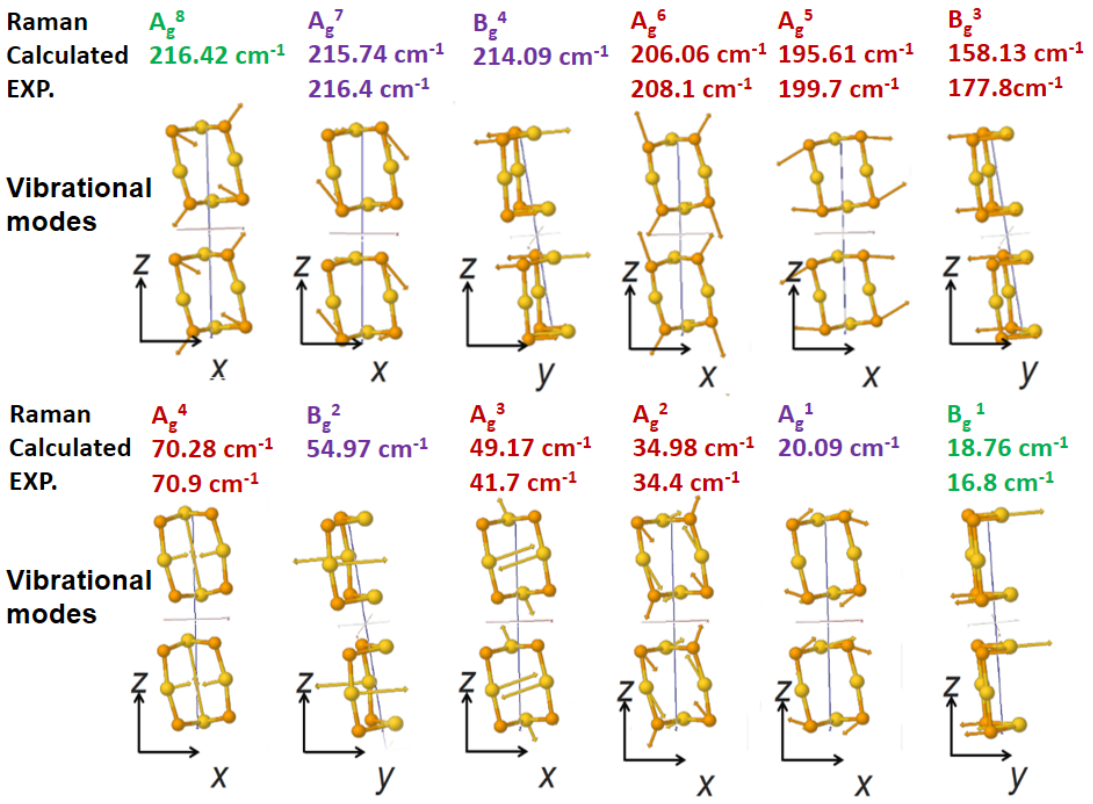

Figure S4. Vibrational modes with Raman activity. The red one represents strong Raman intensity modes, the violet one describes the normal intensity modes, and the green one refers to weak Raman modes. Only B_g^1, A_g^2, A_g^3, A_g^4, B_g^3, A_g^5, A_g^6, A_g^7 can be observed in experiment. The Raman peak at 216.4 cm^{-1} is a mixed peak of Ag^7 and Bg^4.

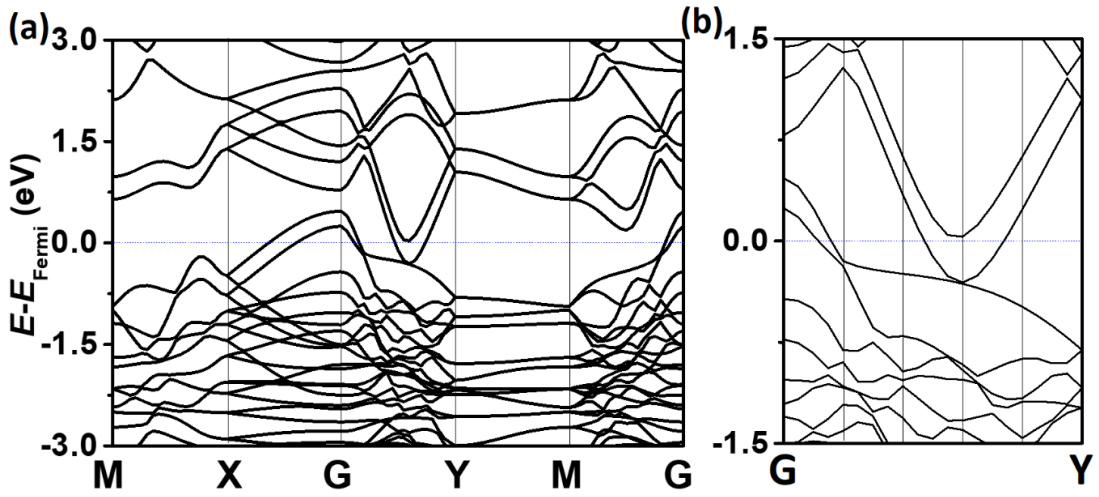

Figure S5. (a) Bandstructure of monolayer AuSe. (b) Bandstructure in the direction of G-Y. The hole and electron pockets overlap in the direction of G-Y, indicating its metallic nature.

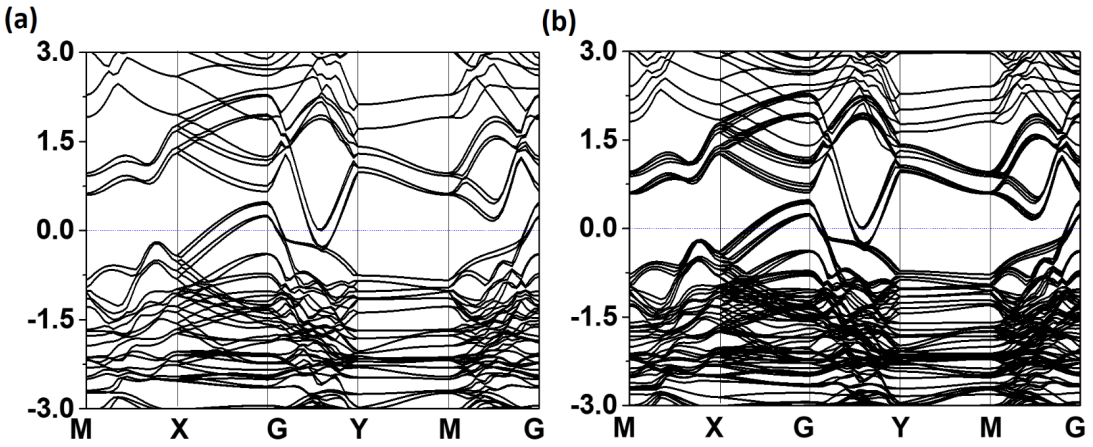

Figure S6. (a) Bandstructure of 2-layer AuSe. (b) Bandstructure of 4-layer AuSe. For both 2-layer and 4-layer AuSe, the hole and electron pockets overlap in the direction of G-Y, indicating similar metallic characteristics of 2-layer and 4-layer AuSe.

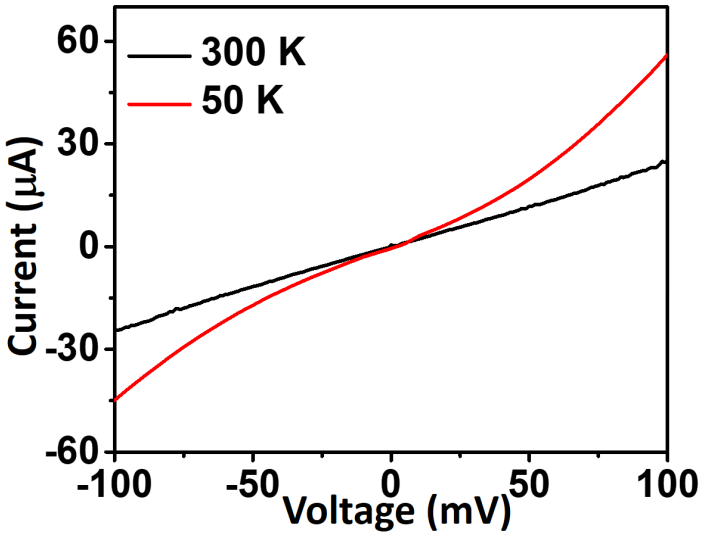

Figure S7. Two terminal I-V curve of the AuSe under 300 K and 50 K. The I-V curve of AuSe is linear at 300 K, while shows slightly nonlinear at 50 K. The two-terminal resistance of AuSe decreases with the decrease of temperature. The I-V curve exhibits nonlinear with the decrease of temperature, which is mainly caused by the electrical contact.

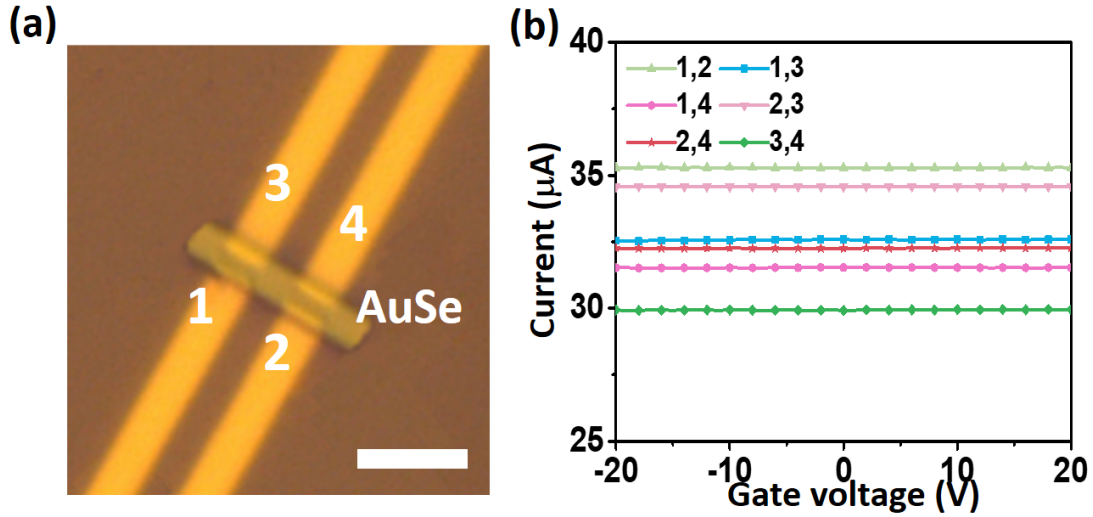

Figure S8. Anisotropic behavior of the AuSe. (a) Optical image of the device. The scale bar is 5 μm (b) Current along different directions of AuSe. The applied bias is 0.1 V. The two-terminal conductivity along the *b*-axis is 1.8 $\times 10^{-3}$ S, and along the *a*-axis is about 1.48×10^{-4} S. Along both the *a*-axis and the *b*-axis, the currents show no gate control, indicating its metallic nature. The high conductivity along the *a*-axis direction indicate that the interaction between AuSe atomic chain is quite strong.

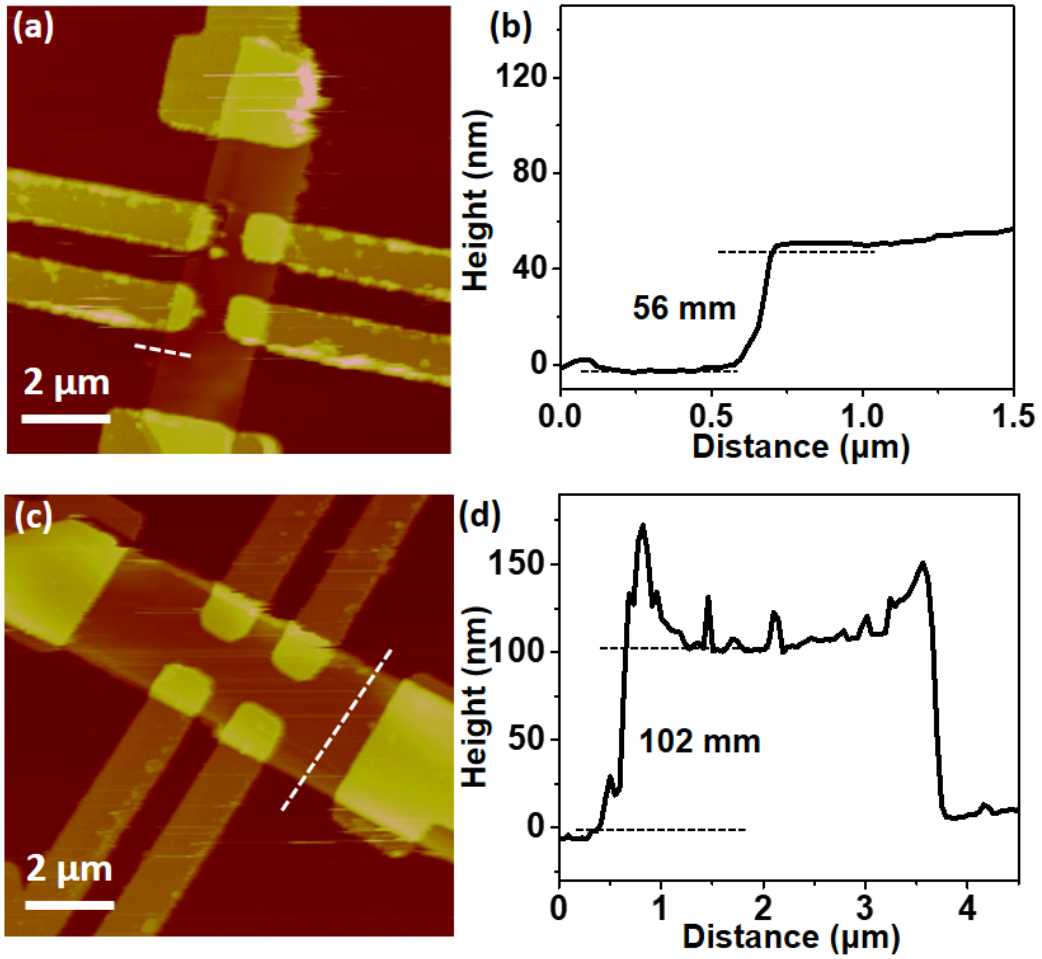

Figure S9. AFM image of the AuSe device with different thickness. Figure S9 (a)-(b) is the AFM image and its height profile tested in Figure 4. The thickness is 56 nm. Figure S9(c)-(d) is the AFM image and its height profile of the sample tested in Figure 5. The thickness of the AuSe is about 102 nm.

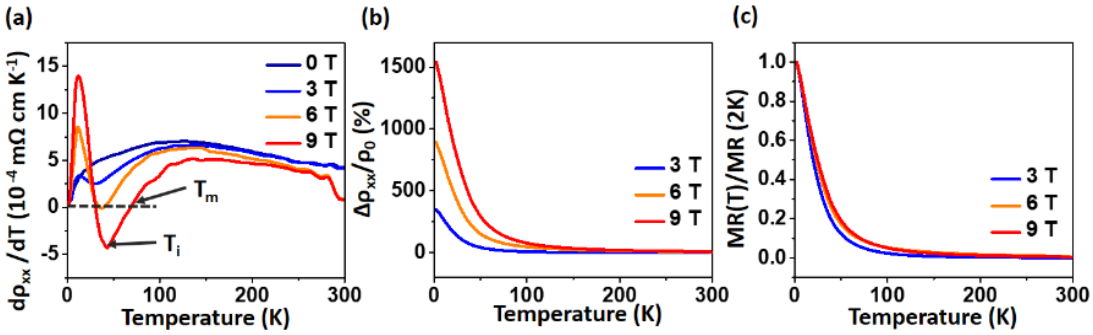

Figure S10. (a) The change rate of ρ_{xx} as a function of temperature T with magnetic field from 0 T to 9 T. (b) The MR as a function of temperature from 3 T to 9 T. (c) The normalized MR as a function of temperature from 3 T to 9 T.

In Figure S10(a), T_m refers to the locations of the resistance minima and T_i indicates the location, where it gradually saturates to a peak. We don't observe a resistance minimal T_m for 0 T and 3 T. T_m becomes larger with the increase of magnetic field. The minima for 6 T and 9 T are 37.4 K and 68.7 K, respectively. Through the position of T_m, we can make a rough estimation of the effective mass $m^* \sim \hbar eB/T_m k_B \sim 0.16\ m_e$. According to DFT calculation, the effective mass of the hole pocket along the G-Y direction is 0.14 m_e and the electron pocket along the G-Y direction is 0.20 m_e, which is in good agreement with our experiment. Although we observe a peak in the ρ_{xx}, we don't find any peak in the plot of MR-temperature. The MR and the normalized MR in Figure **S10(b)-(c)** have the same temperature dependence at different magnetic fields, indicating that the upturn of ρ_{xx} is not caused by the metal-insulator transition.

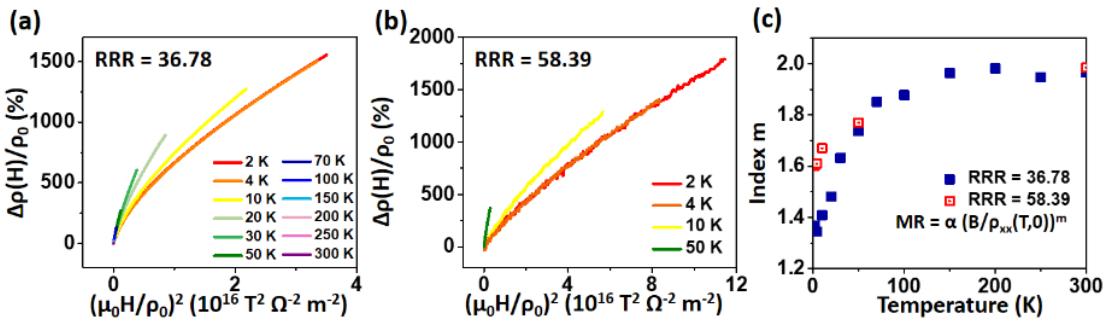

Figure S11. (a-b) A Kohler plot for AuSe with the current parallel to the *y*-axis and the magnetic field perpendicular to the AuSe plane along the *z*-axis. The thickness of this sample is 56 nm and 102 nm. (c) The index m for the Kohler's law.

The residual resistivity ratio (RRR) is defined as RRR= ρ_{xx} (300 K)/ρ_{xx} (2 K). In Figure S11(a), the RRR value of the AuSe is 36.78 and the index m of Kohler's law is 1.36 at 2 K. For the temperature between 70 K and 300 K, the index is close to 2. However, for temperature below 50 K, the MR does not follow the square index. For the sample in Figure S11(b), the index m of Kohler's law is 1.59 at 2 K. The RRR of this AuSe sample is 58.39, indicating better quality and less scattering of the thicker sample. The index *m* as a function of the temperature *T* is given in Figure S11(c). For all the temperature we tested, the Kohler's law index *m* of the 102 nm sample is higher than the one of 56 nm.

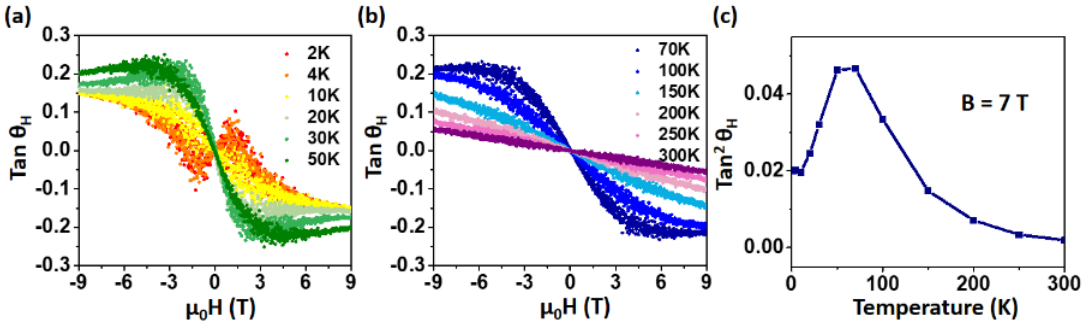

Figure S12. The Hall angle *tan* θ_H for temperature (a) from 2 K to 50 K and (b) from 70 K to 300 K as a function of H. (c) $tan^2\ \theta_H$ measured at $\mu_0 H$ = 7 T as a function of T.

Figure S12(a)-(b) display the $tan\ \theta_H = \rho_{xy}/\rho_{xx}$ as a function of the magnetic field H with different temperature. The *tan* θ_H from 20 K to 70 K shows saturation at about 7 T with the highest values of about 0.2. For the temperature below 2 K and higher than 100 K, the saturation behavior is unnoticeable. Figure S12(c) is the temperature dependence of the $tan^2\ \theta_H$ measured at 7 T. The $tan^2\ \theta_H$ shows a peak at around 70 K and is small within all temperature. It is noteworthy that small Hall angle is usually found in many materials with extreme large magnetoresistance. The Hall conductance σ_{xx} equals $\rho_{xx}/(\rho^2_{xx}+\rho^2_{xy})$ and the longitudinal resistance can be expressed in terms of σ_{xx} and *tan* θ_H :

$$\boldsymbol{\rho_{xx}} = \frac{\boldsymbol{\sigma_{xx}}}{\boldsymbol{\sigma_{xx}^2+\sigma_{xy}^2}} = \boldsymbol{\rho'_{xx}}\left(\frac{\mathbf{1}}{\mathbf{1+tan^2\theta H}}\right), \boldsymbol{\rho'}_{\boldsymbol{xx}} = \frac{\mathbf{1}}{\boldsymbol{\sigma_{xx}}},$$

Since the $tan\theta_H$ is small from 2 K to 300 K, the longitudinal resistance $\rho_{xx} \sim 1/\sigma_{xx}$ at all temperature and the change of it is in accordance of σ_{xx}. The small Hall angle is well consist the band structure of AuSe with nearly compensated semimetal.

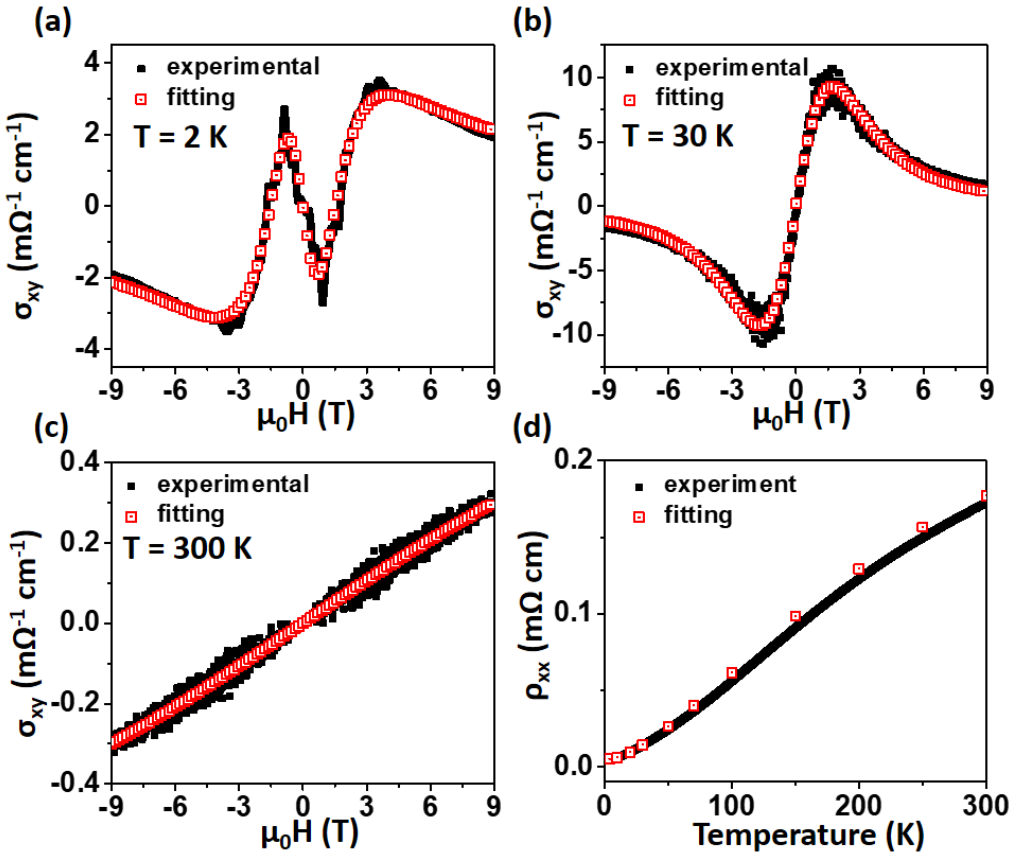

Figure S13. (a)-(c) The σ_{xy} plot as a function of H for AuSe measured at 2 K, 30 K and 300 K. The black dots are the experiment result and the red dots fits to the two band model. (d) The ρ_{xx} plot as a function of temperature. The red dot fitting is calculated using the n_e, n_h, μ_e, μ_h obtained from the σ_{xy} and σ_{xx}.

The Hall conductivity σ_{xy} and longitudinal conductivity σ_{xx} can be written as:

$$\sigma_{xy} = \left(\frac{n_h\mu_h^2}{1+\mu_h^2H^2} - \frac{n_e\mu_e^2}{1+\mu_e^2H^2}\right)eB, \quad (1)$$

$$\sigma_{xx} = \left(\frac{\mu_h n_h}{1+\mu_h^2H^2} + \frac{\mu_e n_e}{1+\mu_e^2H^2}\right)e \quad (2)$$

We force the fit to the σ_{xx} and σ_{xy} and extract the mobility and the carrier density. Then we use the obtained n_e, n_h, μ_e, μ_h to fit the longitudinal resistance ρ_{xx}. The calculated carrier density and mobility fits the ρ_{xx} very well. These results can well explain the compensation of electrons and holes.

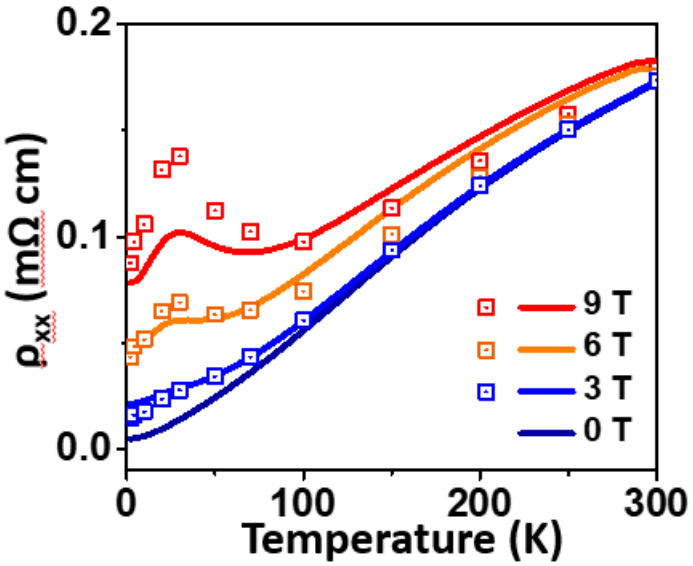

Figure S14. Simulation of the ρ_{xx} assuming $u_h = u_e$. The dots are the simulation when the mobility of electron equals the mobility of holes and the solid line are the experimental result.

For a (nearly) compensated semimetal, the MR can be expressed as:

$$MR = \frac{n_e\mu_e n_h\mu_h(\mu_e+\mu_h)^2(\mu_0 H)^2}{(n_e\mu_e+n_h\mu_h)^2+(n_e-n_h)^2(\mu_e\mu_h)^2(\mu_0 H)^2} \quad (3)$$

For the compensated semimetals, the $MR=\mu_e\mu_h(\mu_0 H)^2$ and the index m of the Kohler's plot is 2. In classical two-band model theory, if we assume the mobility of electron and hole are equal, the longitudinal resistance ρ_{xx} can be written as:

$$\rho_{xx}(\mathrm{T},\mu_0\mathrm{H}) = \rho_{xx}(T,0) + \frac{4\lambda\rho_{xx}(T,0)(\mu_0\mathrm{H})^2}{\frac{1}{4\alpha}\rho_{xx}(T,0)^2(1+\lambda)^4+(\lambda-1)^4(\mu_0\mathrm{H})^2} \quad (4)$$

where $\alpha=[e(n_e + n_h)]^{-2}$ *and* $\lambda= n_e/n_h$, respectively. Since we want to study the effect of the carrier density, we just take the carrier density into the simulation. Both of the upturn and the reentrant metallic behavior are observed in this sample. If the carriers are well compensated, it will follow the Kohler's law perfectly under all temperature and the reentrant metallic behavior will disappear. Based on this simulation, we can conclude that the upturn behavior is mainly caused by the electron hole compensation from 70 K to 300 K, and the reentrant metallic behavior is caused by the small n_e/n_h mismatch from 2 K to 50 K.

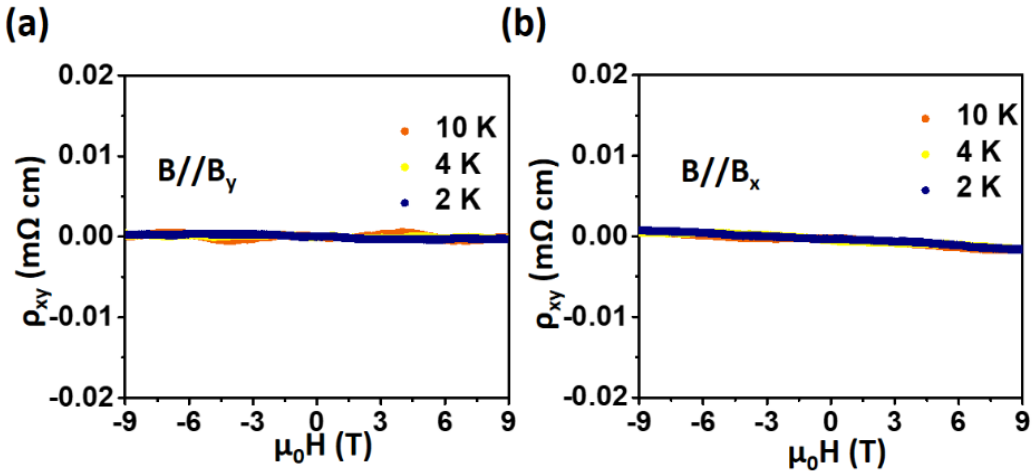

Figure S15. ρ_{xy} of AuSe device with the magnetic field along the B_y and B_x direction.

Table S1. Calculated and experimental vibrational Raman frequencies of primitive α-AuSe.

Mode	VASP	VASP-rescale	QE	Experiment
A_g^8	209.96	216.42	218.61	
A_g^7	209.30	215.74	222.98	216.42
B_g^4	207.70	214.09	215.97	
A_g^6	199.91	206.06	205.96	208.14
A_g^5	189.78	195.61	197	199.68
B_g^3	153.41	158.13	170.41	177.81
A_g^4	68.18	70.28	68.77	70.9
B_g^2	53.33	54.97	60.53	
A_g^3	47.70	49.17	55.42	41.7
A_g^2	33.93	34.98	34.13	34.4
A_g^1	19.49	20.09	22.99	
B_g^1	18.20	18.76	18.23	16.8